



HAL
open science

Forced oscillation measurements of seismic wave attenuation and stiffness moduli dispersion in glycerine-saturated Berea sandstone

Samuel Chapman, Jan V. M. Borgomano, Hanjun Yin, Jerome Fortin, Beatriz Quintal

► **To cite this version:**

Samuel Chapman, Jan V. M. Borgomano, Hanjun Yin, Jerome Fortin, Beatriz Quintal. Forced oscillation measurements of seismic wave attenuation and stiffness moduli dispersion in glycerine-saturated Berea sandstone. *Geophysical Prospecting*, 2018, 10.1111/1365-2478.12710 . hal-02350569

HAL Id: hal-02350569

<https://hal.science/hal-02350569v1>

Submitted on 6 Nov 2019

HAL is a multi-disciplinary open access archive for the deposit and dissemination of scientific research documents, whether they are published or not. The documents may come from teaching and research institutions in France or abroad, or from public or private research centers.

L'archive ouverte pluridisciplinaire **HAL**, est destinée au dépôt et à la diffusion de documents scientifiques de niveau recherche, publiés ou non, émanant des établissements d'enseignement et de recherche français ou étrangers, des laboratoires publics ou privés.

1 **Forced oscillation measurements of seismic wave attenuation and stiffness moduli**
2 **dispersion in glycerine-saturated Berea sandstone**

3

4 Samuel Chapman^{1,2} (samuel.chapman@unil.ch), Jan V. M. Borgomano², Hanjun Yin^{2,3},
5 Jerome Fortin², and Beatriz Quintal¹

6

7 1) Institute of Earth Sciences, University of Lausanne, Lausanne, Switzerland.

8 2) Laboratoire de Géologie, Ecole Normale Supérieure / CNRS UMR 8538, PSL Research
9 University, Paris, France.

10 3) State Key Laboratory of Petroleum Resources and Prospecting, China University of
11 Petroleum-Beijing, Beijing, China.

12

13 **Abstract**

14 Fluid pressure diffusion occurring on the microscopic scale is believed to be a significant
15 source of intrinsic attenuation of seismic waves propagating through fully saturated porous
16 rocks. The so-called squirt flow arises from compressibility heterogeneities in the
17 microstructure of the rocks. To study squirt flow experimentally at seismic frequencies the
18 forced oscillation method is the most adequate, but these studies are still scarce. Here we
19 present the results of forced hydrostatic and axial oscillation experiments on dry and
20 glycerine-saturated Berea sandstone, from which we determine the dynamic stiffness moduli
21 and attenuation at micro-seismic and seismic frequencies (0.004 – 30 Hz). We observe
22 frequency-dependent attenuation in response to the drained-undrained transition (~0.1 Hz)
23 and squirt flow (>10 Hz). The frequency-dependent attenuation and associated modulus
24 dispersion at 5 MPa effective stress is in fairly good agreement with the results of the
25 analytical solutions for the drained-undrained transition and squirt flow. The comparison with

26 very similar experiments performed also on Berea sandstone indicates that squirt flow can
27 potentially be a source of seismic wave attenuation across a large range of frequencies
28 because of its sensitivity to small variations in the rock microstructure, especially in the
29 aspect ratio of micro-cracks or grain contacts.

30

31 **Key Words**

32 - Attenuation

33 - Rock physics

34

35 **1. Introduction**

36

37 Porous rocks saturated with fluids can strongly attenuate seismic waves. Different forms of
38 wave-induced fluid flow (WIFF) are thought to be the primary intrinsic mechanism for
39 seismic wave attenuation (e.g. Pride *et al.* 2004). Fluid flow arises predominantly from
40 contrasts in compressibility either in the solid matrix of the rock, for instance between
41 compliant grain contacts and stiff pores, or in the saturating fluids, such as a heterogeneous
42 distribution of water and gas. In response to such compressibility contrasts, seismic waves
43 induce pressure gradients, resulting in viscous fluid flow and the conversion of the waves
44 mechanical energy into heat. The frequency dependence of the associated seismic attenuation
45 depends strongly on the spatial distribution or geometry of the heterogeneities in the rock
46 matrix and/or in the saturating fluids (Masson and Pride 2007, 2011; Müller *et al.* 2008). A
47 direct consequence of the frequency dependent attenuation is that the corresponding stiffness
48 modulus of the rock will also be frequency dependent.

49

50 Much focus has been given to squirt flow, pressure diffusion arising from microscopic
51 compressibility heterogeneities in the rock, as one of the dominant mechanisms for wave
52 attenuation in fluid saturated rocks. Numerous theoretical models (e.g. O'Connell and
53 Budiansky 1977; Mavko and Jizba 1991; Chapman *et al.* 2002; Gurevich *et al.* 2010; Adelinet
54 *et al.* 2011) have been developed to try to explain laboratory observations at sonic and
55 ultrasonic frequencies. More recently, with the progress made in using the forced oscillation
56 method (e.g. McKavanagh and Stacey 1974), squirt flow has been studied also at seismic
57 frequencies by using high viscosity fluids such as glycerine.

58

59 On a Fontainebleau sandstone sample saturated with glycerine, Pimienta *et al.* (2015a)
60 observe an extensional mode attenuation peak at between 1 and 10 Hz, which was reduced in
61 amplitude with increasing effective stress. Subramanyan *et al.* (2015) also measured the
62 extensional mode attenuation and Young's modulus in Fontainebleau sandstone with similar
63 properties, in this case varying the fluid viscosity by mixing water and glycerine. For the fully
64 glycerine-saturated sample they observe an attenuation peak in a similar frequency range and
65 with similar amplitude, supporting the observation of Pimienta *et al.* (2015a). In addition
66 Subramanyan *et al.* (2015) used Gurevich *et al.*'s (2010) analytical solution of squirt flow to
67 interpret their observations, however the analytical solution consistently underestimated the
68 attenuation magnitude measured in the laboratory. The broad attenuation peaks observed were
69 attributed to a distribution of crack aspect ratios.

70

71 In a glycerine saturated Berea sandstone sample Mikhaltsevich *et al.* (2015; 2016) measured
72 the dynamic Young's modulus and Poisson ratio, from which they inferred the bulk and shear
73 moduli as well as the corresponding attenuation modes. By performing measurements at
74 temperatures from 31 to 23 °C, they observe a shift of the extensional-mode attenuation peak

75 from ~ 2 to ~ 0.4 Hz, associated with the reduction of the glycerine viscosity. Mikhaltsevtich
76 *et al.* (2015) interpreted the attenuation as being caused by squirt flow. Spencer and Shine
77 (2016) also performed forced oscillation experiments on a fully saturated Berea sandstone
78 sample, however only observing a partial attenuation curve. Similar to Mikhaltsevtich *et al.*
79 (2016) the impact of fluid viscosity was studied, however instead of modifying the
80 temperature, fluids of varying degrees of viscosity were used. Pimienta *et al.* (2017)
81 investigated frequency-dependent attenuation and modulus dispersion in four different types
82 of sandstone, including Berea sandstone, under full water and glycerine saturation. In the
83 Wilkenson and Bentheim sandstones both showed frequency dependent attenuation likely in
84 response to squirt-flow, showing a strong sensitivity to changes in effective pressure.
85 However in the Berea sandstone samples the presence of squirt flow could not be verified in
86 the considered frequency range.

87
88 Even though there has been a recent surge in the availability of laboratory data from fully
89 saturated sandstones at seismic frequencies (<100 Hz), the overall understanding of the
90 physical processes responsible for the frequency-dependent attenuation and modulus
91 dispersion remains incomplete. Comparing experiments is especially challenging given the
92 variation in microstructure between samples and the use of a range of different saturating
93 fluids. Furthermore the analysis is considerably complicated by the impact or not of boundary
94 conditions on the observed frequency-dependent attenuation, which is associated with the
95 design of the experimental apparatus (e.g., Pimienta *et al.*, 2016).

96
97 To contribute to the available data, we present in the following sections the results of forced
98 hydrostatic and axial oscillation experiments on a Berea sandstone sample. The experiments
99 were performed on the dry and fully glycerine-saturated sample for a range of effective

100 stresses. We will provide a description of the sample and the experimental conditions. The
101 discussion of our results for the dispersion of the stiffness moduli and corresponding
102 attenuation modes will focus on the uncertainty in our measurements, the physical processes
103 responsible for our observations, how the theoretical predictions compare to our observations,
104 and how our observations compare to those of Mikhaltsevtich *et al.* (2016), whose
105 experiments are the most similar to ours.

106

107 **2. Samples and experimental methodology**

108

109 2.1 Sample description

110

111 Three samples with a ~4 cm diameter and ~8 cm length were cored from a block of Berea
112 sandstone with poorly defined bedding planes, running parallel to the samples vertical axis.
113 The Berea sandstone was acquired from Cleveland Quarries in the United States with a brine
114 permeability estimated at 75 to 250 mD. The glycerine permeability of sample BS-V5 was
115 subsequently measured at an effective stress of 2.5 MPa by imposing a pressure gradient
116 across the sample and measuring the associated flow. The porosity was determined with a
117 pyknometer, using a subsection of sample BS-V6. The dry density is the mean density
118 determined from the dry masses and dimensions of the three samples. These properties are
119 listed in Table 1. Scanning electron microscopy (SEM) and energy dispersion spectrometry
120 (SEM-EDS) analysis (Figure 1) shows that our sample is composed largely of quartz (Si),
121 with smaller amounts feldspar and clays (Al) [can we be more precise and give the
122 composition according Fig1?]. Kareem et al. (2017) performed an extensive characterisation
123 of Berea sandstone cores, also purchased from Cleveland Quarries, showing that clays make
124 up between 3 and 9 % of the bulk composition, with the predominant clay being kaolinite.

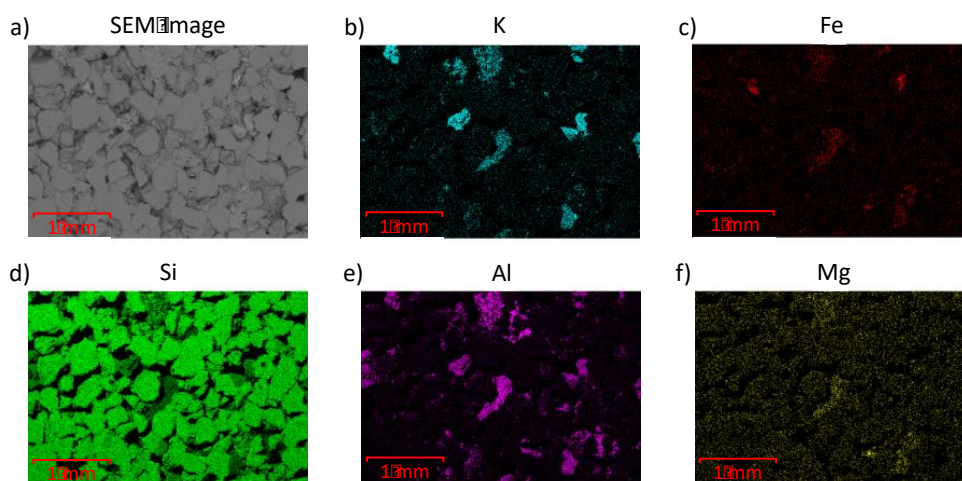
125

126 **Table 1.** Sample properties

	BS-V4 to BS-V6
Glycerine Permeability (mD)	$58.7 \pm 1.14^*$
Porosity (%)	22.15
Dry Density (kg/m^3)	2087 ± 6.55

127 * Measured at 2.5 MPa effective stress.

128



129

130 **Figure 1.** a) Scanning electron microscopy (SEM) image of the polished surface of BS-V6.
131 Energy dispersion spectrometry (EDS-SEM) images of the same sample portion showing the
132 distribution of b) potassium (K), c) iron (Fe), d) silicon (Si), e) aluminium (Al) and f)
133 magnesium (Mg).

134

135 2.2 Experimental setup - dynamic moduli and attenuation modes

136

137 Forced oscillation measurements were performed in a tri-axial cell at ENS Paris. Borgomano
138 *et al.* (2017) provide a detailed description of the experimental setup and data processing.
139 Pimienta *et al.* (2015a,b) provide further details on the calibration of the apparatus with

140 standard materials. We will briefly list the governing relations used to determine the various
141 moduli and associated attenuation modes.

142

143 Two types of stress oscillation on the sample, producing strains on the order of $\sim 10^{-6}$, can be
144 performed in this cell: hydrostatic and axial. The hydrostatic oscillation (4×10^{-3} to ~ 1 Hz) is
145 induced by the confining pressure pump (Adelinet *et al.* 2010; David *et al.* 2013) and allows
146 for directly measuring the sample's dynamic bulk modulus from the confining pressure
147 oscillation $\Delta P_c = -\sigma_{ii}/3$, where σ_{ii} ($i = 1,2,3$) are the principal stresses, and the associated
148 volumetric strain ϵ_{vol} as follows: [In formula 1, we don't need the negative sign, if we
149 consider E_{vol} positive in compaction]

$$150 \quad K_{hydro} = \frac{-DP_c}{\epsilon_{vol}}. \quad (1)$$

151 The volumetric strain is determined from the average strain measured by 8 strain gauges,
152 comprising four pairs of radial and axial strain gauges, as $\epsilon_{vol} = 3\epsilon_{avg}$.

153

154 The axial oscillation (1×10^{-1} to ~ 20 Hz) is induced by a piezo-electric actuator placed
155 between the sample and the axial piston of the cell and allows for measuring the sample's
156 Poisson ratio ν and Young's modulus E :

$$157 \quad \nu = -\frac{\epsilon_{rad}}{\epsilon_{ax}} \text{ and } E = \frac{S_{ax}}{\epsilon_{ax}}, \quad (2)$$

158 where the axial stress σ_{ax} , is determined from the deformation of the aluminium end plate of
159 known Young's modulus, and ϵ_{rad} and ϵ_{ax} are the average radial and axial strains on the
160 sample. Given the Poisson ratio and Young's modulus, the axial bulk K_{ax} and shear G_{ax}
161 moduli can be inferred as follows:

162 $K_{ax} = \frac{E}{3(1-2n)}$ and $G_{ax} = \frac{E}{2(1+n)}$. (3)

163

164 For each mode of deformation, the attenuation can be determined from the phase shift
 165 between the applied stress and resulting strain ($\Delta\phi = \phi_{\text{stress}} - \phi_{\text{strain}}$). The bulk attenuation for
 166 the hydrostatic oscillation can be determined from the phase shift between the hydrostatic
 167 stress ΔP_c and the volumetric strain ε_{vol} , such that:

168 $Df_{hydro} = f_{-DP_c} - f_{\varepsilon_{vol}}$. [Here again, the negative sign in P_c is not useful]

169 (4)

170 The extensional mode attenuation is in turn determined from the phase shift between the axial
 171 stress σ_{ax} and strain ε_{ax} , such that:

172 $Df_{extensional} = f_{\sigma_{ax}} - f_{\varepsilon_{rad}}$. (5)

173 Assuming that the sample is isotropic, the bulk and shear attenuation can be inferred from the
 174 phase shift between the axial stress σ_{ax} and the axial and radial strains ε_{ax} and ε_{rad} (Borgomano
 175 *et al.* 2017):

176 $Df_{bulk} = f_{\sigma_{ax}} - f_{\varepsilon_{ax} + 2\varepsilon_{rad}}$ and $Df_{shear} = f_{\sigma_{ax}} - f_{\varepsilon_{ax} - \varepsilon_{rad}}$, (6)

177 where the phases of $\varepsilon_{ax} + 2\varepsilon_{rad}$ and $\varepsilon_{ax} - \varepsilon_{rad}$ are derived from combining equations 2 and 3.

178 The attenuation corresponding to each deformation mode can be calculated as (O'Connell and
 179 Budiansky 1978):

180 $Q^{-1} = \tan(Df)$. (7)

181

182 2.3 Experimental conditions

183

184 Axial and hydrostatic oscillations, were performed on the dry and glycerine-saturated sample
185 (BS-V5). Axial oscillations were performed at effective stresses between 2.5 and 25 MPa,
186 with an additional static axial load of 2 MPa. We will refer to the effective stress as the
187 difference between the confining and fluid pressure, $\sigma_{\text{eff}} = P_c - P_f$. The static axial load is
188 applied to ensure coupling between the sample and the piezoelectric actuator. The hydrostatic
189 oscillations were performed for the same range of effective stresses, however without
190 imposing an additional static axial load. Before saturating the sample with glycerine, a
191 vacuum pump was used to remove air from its pore space. Glycerine was then pumped into
192 the sample using two Quizix pumps that subsequently regulated the fluid pressure at 4 MPa.

193

194 **3. Results and Discussion**

195 3.1 Measurement Uncertainty

196

197 To assess the uncertainty in our measured frequency-dependent moduli and attenuation we
198 look at the repeatability of the measurements and the variation of the data with respect to an
199 idealized model. The moduli and attenuation are inferred from the strain measured on the
200 sample. For hydrostatic forced oscillations we have eight measurements of strain, while for
201 axial forced oscillations we have a pair of averages consisting of two axial and radial
202 measurements of strain on opposing sides of the sample. We determine the repeatability of
203 our moduli and attenuation for hydrostatic oscillations by taking the standard deviation over
204 the eight measurements of strain. In the case of the axial oscillations we only have two
205 measurements of each moduli and its corresponding attenuation, we therefore estimate the
206 repeatability of our measurements from their range. To assess the variation of our data with
207 respect to an idealized model we follow Adam et al.'s (2006) procedure of fitting a linear

208 function of $\log_{10}(\text{frequency})$ to the mean of our measured data and determining the root-
209 mean-squared-error (RMSE).

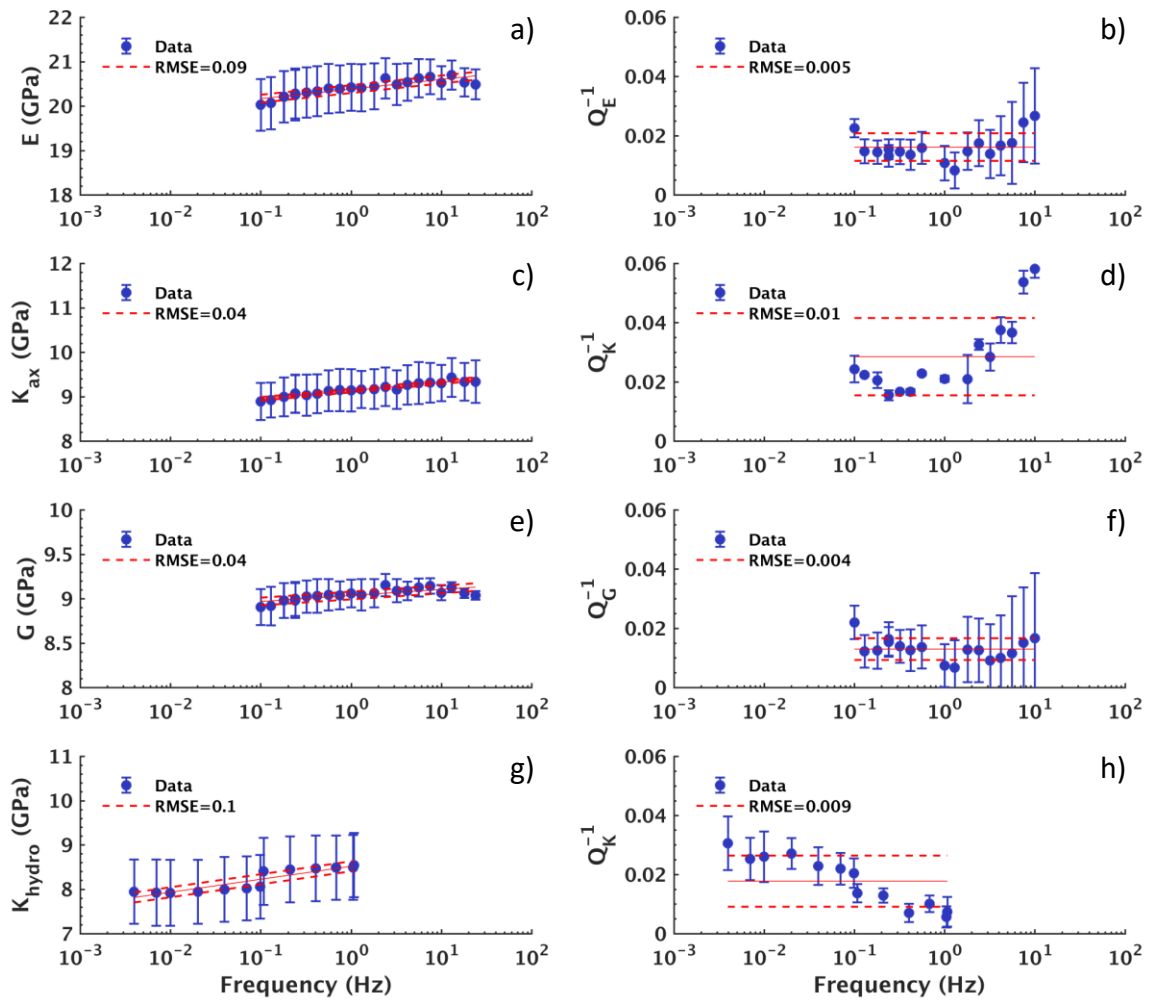
210

211 Figure 2 shows the moduli and corresponding attenuation inferred from axial and hydrostatic
212 oscillations performed on the dry sample at 5 MPa effective stress. The moduli increase
213 moderately towards higher frequencies and the measurement range generally exceeds the
214 variation of the measurement mean around the fit. For the corresponding attenuation the
215 measurement range is much more variable and, for the Young's and shear components, it
216 increases towards higher frequencies. Attenuation is only shown up to 10 Hz, because at
217 higher frequencies it strongly deviates from the fitting trend (Figure 2b, d and f). The
218 measurement range appears to largely over estimate our uncertainty, however it also shows
219 that the uncertainty is not independent of frequency. In the following sections we will
220 therefore present the range when error bars are displayed.

221

222

223



224

225 **Figure 2.** Frequency-dependent moduli and corresponding attenuation inferred from axial and
 226 hydrostatic forced oscillations on the dry sample at 5 MPa effective stress. The data points
 227 represent the mean measurement and the error-bars indicate the range of the measurements
 228 for axial oscillations (a – f) and the standard deviation in the measurements for hydrostatic
 229 oscillations (g – h). A linear function of $\log_{10}(\text{frequency})$ is fit to the data and the root-mean-
 230 squared-error (RMSE) is indicated in the legend.

231

232 3.2 Frequency dependence – glycerine saturation

233

234 When the sample is glycerine saturated all modes show significant frequency dependent
235 attenuation (Figures 3a, 4a and 5a). For the extensional (Figure 3a) and bulk attenuation
236 (Figure 4a) two peaks are observed: one at ~ 0.1 Hz and another beginning at ~ 3 Hz and
237 above. For the shear attenuation (Figure 5a) however only the attenuation peak at higher
238 frequencies is observed. The attenuation peak at ~ 0.1 Hz is reduced in amplitude as the
239 effective stress is increased. The second partial peak at higher frequencies is likewise reduced
240 in amplitude, however at 15 MPa effective stress the measured attenuation is comparable in
241 amplitude to the attenuation measured for the dry sample.

242

243 As with the attenuation the various stiffness moduli are frequency-dependent once the sample
244 is saturated with glycerine (Figures 3b, 4b and 5b). The overall increase in the sample's
245 stiffness from dry to glycerine saturated is particularly observed in the Young's modulus
246 (Figure 3b). The shear modulus at low frequencies is on the order of the shear modulus of the
247 dry sample (Figure 5b). Towards higher frequencies the shear modulus shows some
248 dispersion. The Young's and bulk moduli are dispersive at both ~ 0.1 Hz and again beginning
249 at ~ 3 Hz. Overall the moduli become less dispersive with increasing effective stress. At high
250 frequencies the bulk modulus possibly converges to a common limit. The Poisson ratio
251 (Figure 3c) is significantly increased with respect to the Poisson ratio measured in the dry
252 sample and is frequency dependent (Figure 3c). For the saturated sample, with increasing
253 effective stress the Poisson ratio is reduced and at high frequencies it is nearly frequency
254 independent.

255

256 Because the stress applied to the sample for the hydrostatic oscillation is determined from a
257 pressure transducer close to the sample in the confining oil, while for the axial oscillation the
258 stress it is determined from the deformation of the aluminium end plate on which the sample

259 is placed, the bulk modulus and attenuation can be measured independently by these two
260 methods. If the sample BS-V5 is in fact isotropic then the bulk modulus and attenuation
261 measured by these two methods should be the same. In Figure 4 we show the bulk modulus
262 and attenuation determined from both the hydrostatic and axial oscillations. We observe that
263 the bulk modulus and attenuation are generally independent of the measurement type.
264 However as the effective stress is increased the hydrostatic measurements do show a slightly
265 higher bulk modulus than the axial measurements.

266

267 In the dry measurements our measurement uncertainty increased with frequency and we
268 observed significant frequency dependent attenuation above 10 Hz, indicating misalignments
269 in the experimental set up or an inability of the piezo-electric actuator to generate a sinusoidal
270 signal. To verify the quality of our measurements on the glycerine-saturated sample we
271 therefore make use of the Kramers-Kronig relations to check for the causality between our
272 measured attenuation and moduli. We perform a linear interpolation to the attenuation and
273 apply the Kramers-Kronig relations given by Mikhaltsevitch *et al.* (2016). We do this for the
274 bulk (Figure 4) and shear (Figure 5) components and observe a satisfactory fit between the
275 moduli and the respective attenuation.

276

277 The attenuation peak observed at ~ 0.1 Hz is caused by the drained-undrained transition,
278 which is a boundary condition problem of fluid saturated samples. The forced oscillation of
279 the sample induces fluid pressure diffusion from the sample into the connecting pore fluid
280 lines. The diffusion of pore fluid pressure can be described in terms of a pseudo-skempton
281 coefficient, defined as (Pimienta *et al.* 2015b):

$$282 \quad B^* = \frac{Dp_f}{DP_c}, \quad (10)$$

283 where Δp_f is the fluid pressure amplitude measured in the pore fluid line and ΔP_c is the
284 confining pressure amplitude. In Figure 4c we see that the pseudo-skempton coefficient is
285 elevated at low frequencies, indicating that the glycerine had enough time to flow in response
286 to the confining pressure oscillation and raise the pressure in the pore fluid lines. At low
287 frequencies (0.01 Hz) the sample can therefore be considered partially drained. The pseudo-
288 skempton coefficient approached zero as the frequency of the confining pressure oscillation
289 increases, because the fluid no longer has the time to diffuse from the sample and raise the
290 pressure in the pore fluid lines. At high frequencies (1 Hz) the sample is therefore undrained.
291 Increasing the effective stress increases the sample stiffness, which means that a larger
292 portion of the load is carried by the frame of the sample and not transferred to the fluid. The
293 consequence of increasing the effective stress is that the pseudo-skempton coefficient is also
294 reduced, which is consistent with the observations of Hart and Wang (1999) for the variation
295 of the Skempton's coefficient with effective stress for Berea sandstone.

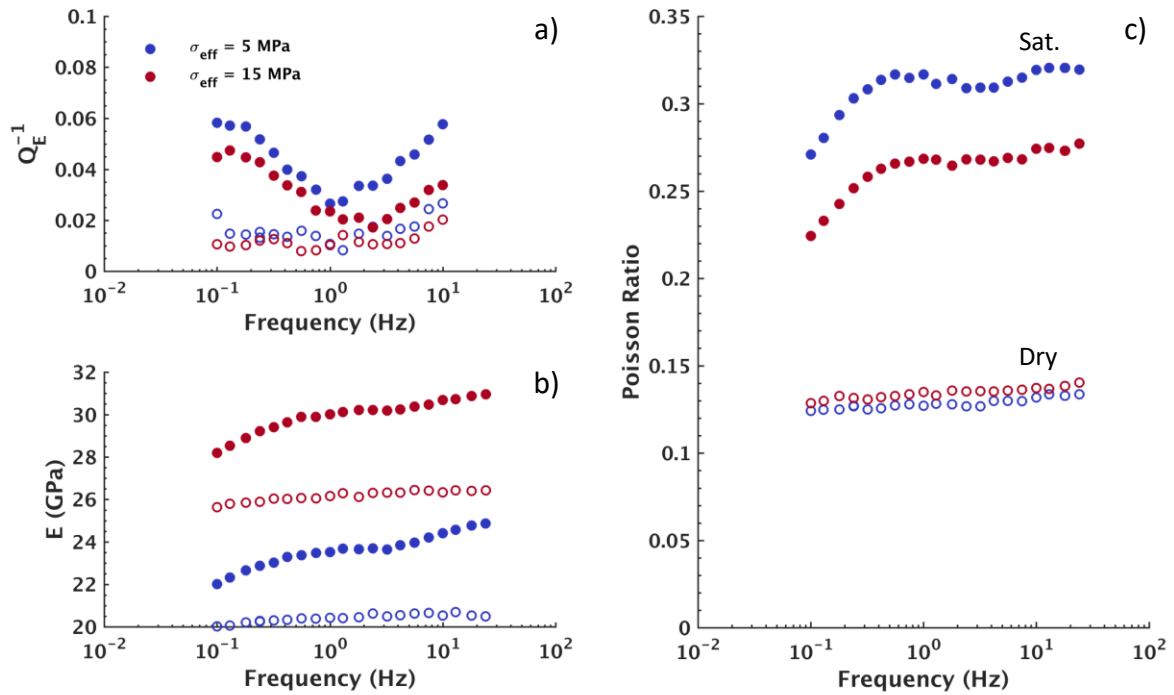
296

297 The second partial attenuation peak observed at above ~ 3 Hz on the other hand is likely in
298 response to squirt flow arising from microscopic compressibility heterogeneities in the rock.
299 This is indicated in part by the sensitivity of the measured attenuation to an increase in
300 effective stress resulting in a reduction of the compliant porosity and a corresponding
301 reduction in attenuation. Indicative of squirt flow is also the dispersion in the shear modulus
302 and corresponding attenuation, which is not the case for attenuation associated with the
303 drained-undrained transition (Figure 5).

304

305

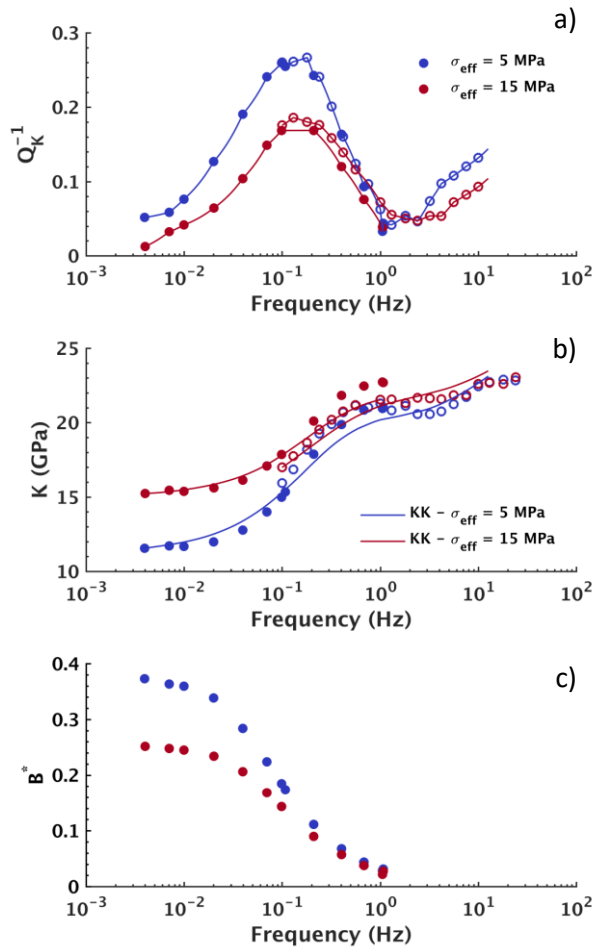
306



307

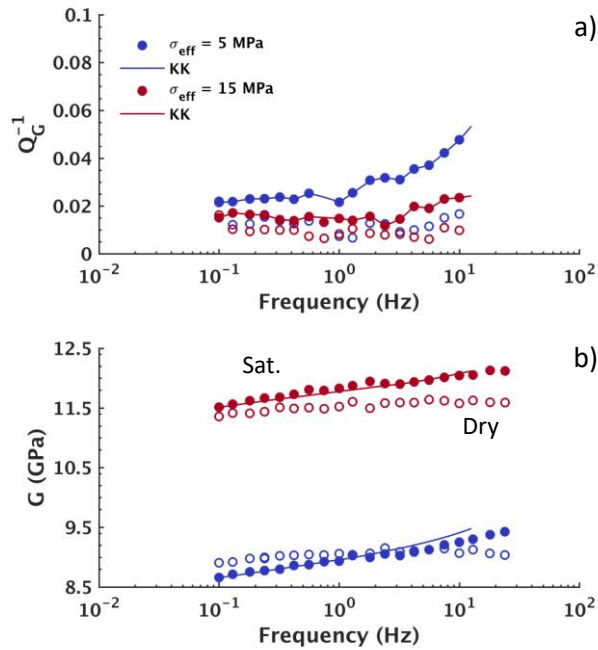
308 **Figure 3.** a) Extensional attenuation Q_E^{-1} , b) Young's modulus E and c) Poisson ratio for the
 309 dry and glycerine-saturated sample BS-V5 inferred from forced axial oscillations. The sample
 310 was subjected to a static axial stress of 2 MPa. The legend provides the applied effective
 311 stress σ_{eff} . Open symbols indicate the dry sample and filled symbols indicate glycerine-
 312 saturated sample.

313



314
 315 **Figure 4.** a) Attenuation Q_K^{-1} , b) bulk modulus K and c) the Pseudo-Skempton coefficient B^*
 316 for the glycerine-saturated sample BS-V5 determined from forced axial (open symbols) and
 317 hydrostatic oscillations. Also shown are the results of Kramers-Kronig (KK) relations
 318 determined from a cubic spline fit to the measured attenuation. For the axial oscillations the
 319 sample was subjected to a static axial stress of 2 MPa. The legend provides the applied
 320 effective stress σ_{eff} .

321



322

323 **Figure 5.** a) Attenuation Q_G^{-1} and b) shear modulus G for the dry and glycerine-saturated
 324 sample BS-V5 determined from forced axial oscillations. Also shown are the results of
 325 Kramers-Kronig (KK) relations. The sample was subjected to a static axial stress of 2 MPa.
 326 The legend provides the applied effective stress σ_{eff} . Open symbols indicate the dry sample
 327 and filled symbols indicate the glycerine-saturated sample.

328

329

330 3.3 Drained-undrained transition and squirt flow

331

332 A number of analytical solutions have been developed to explain modulus dispersion and
 333 attenuation related to squirt flow (e.g. Mavko and Jizba 1991; Chapman *et al.* 2002). Here we
 334 will use Gurevich *et al.*'s (2010) analytical solution which describes the pressure diffusion
 335 between compliant and stiff pores for an oscillating stress. At low frequencies the solution
 336 converges to Gassmann's (1951) undrained limit and at high frequencies converges to Mavko
 337 and Jizba (1991) unrelaxed limit. The analytical solution assumes that the rock is isotropic,
 338 making it applicable to sample BS-V5, with penny shaped cracks having a uniform aspect

339 ratio. To investigate the drained-undrained transition we will in turn use the 1-D analytical
340 solution from Pimienta *et al.* (2016) for the fluid pressure diffusion along the vertical axis of a
341 sample subjected to a hydrostatic pressure oscillation. At high frequencies the solution
342 converges to Gassmann's (1951) undrained limit.

343

344 The input parameters for both models are given in Tables 2 and 3 and correspond to a sample
345 subjected to an effective stress of 5 MPa. The drained bulk and shear moduli are measured
346 from the forced axial oscillations on the dry sample. The compliant porosity, ϕ_c , was
347 estimated from the volumetric strain measured on the dry sample, following the procedure
348 described in Appendix A of Gurevitch *et al.* (2010). The high pressure bulk modulus required
349 by the squirt flow model corresponds to the bulk modulus measured at 25 MPa confining
350 pressure from the forced axial oscillations on the dry sample. The aspect ratio of the
351 compliant cracks cannot be accurately determined from the mechanical and SEM data and is
352 therefore used as a fitting parameter, as it only impacts the frequency dependence. However,
353 an order of magnitude estimation of the aspect ratio can be obtained from Walsh (1965):

354
$$a \gg \frac{4P_{closure}(1-n^2)}{\rho E}, \quad (11)$$

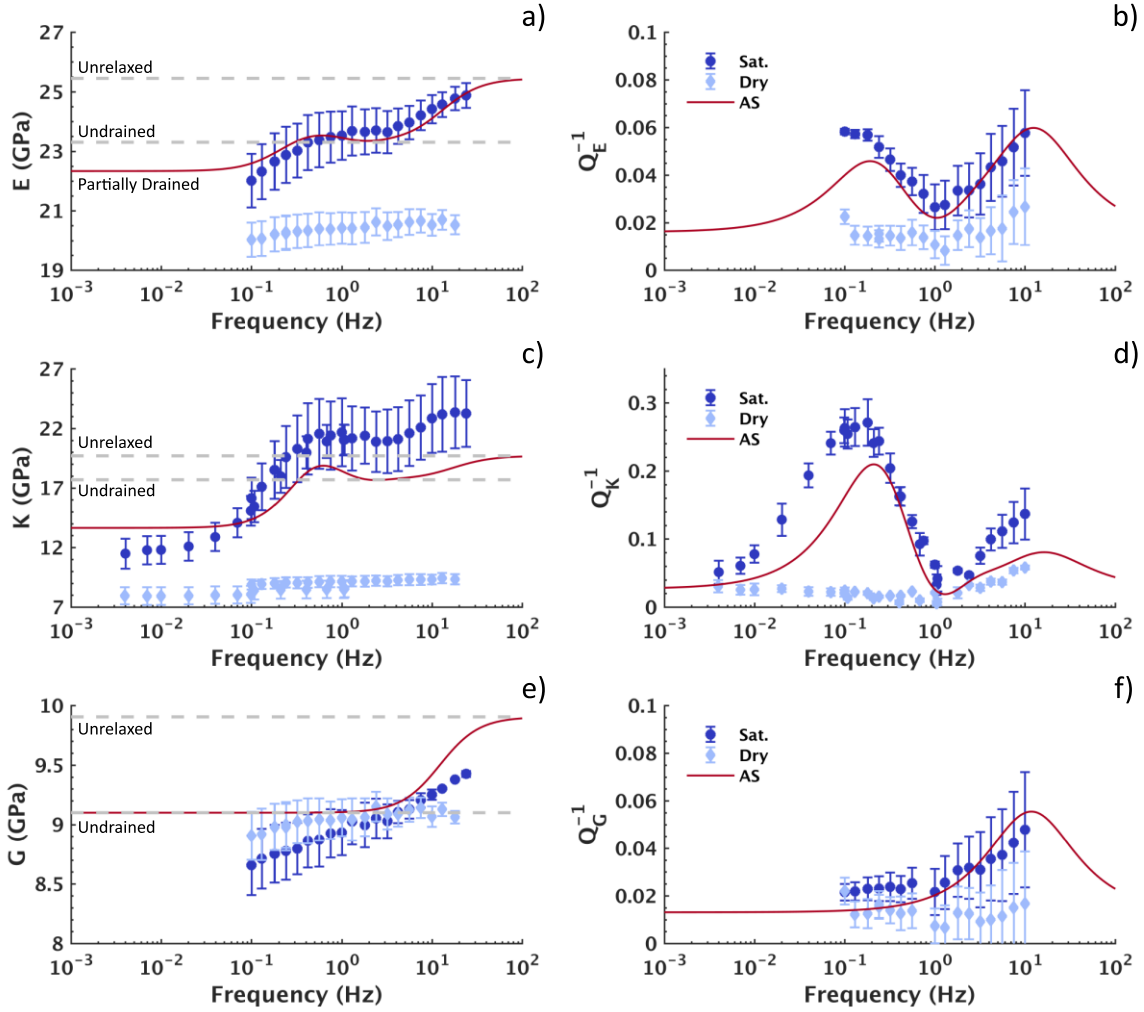
355

356 where $P_{closure}$ is the confining pressure at which the compliant cracks closed in the dry sample,
357 while E is the Young's modulus and ν is the Poisson's ratio. Considering a closure pressure of
358 around 25 MPa, at which we measured a Young's modulus of ~28 GPa and Poisson's ratio of
359 ~0.14, we can infer that the characteristic aspect ratio should be on the order of $\sim 1 \times 10^{-3}$,
360 which is consistent with our choice of aspect ratio (Table 4).

361

362 Figure 6 shows the combined result of the two analytical models together with the moduli and
363 attenuation measured on the dry and glycerine-saturated sample at 5 MPa effective stress.
364 Neither model accounts for the attenuation resulting from frictional dissipation along grain
365 contacts, therefore the attenuation measured in the dry sample is added to the model result
366 (Tisato and Quintal 2013; 2014). The Young's modulus (Figure 6a) and attenuation (Figure
367 6b) derived from the models reproduce well the laboratory observation, while for the bulk
368 modulus dispersion (Figure 6c) and attenuation (Figure 6d) are slightly underestimated. The
369 shear modulus measured in the glycerine-saturated sample is reduced relative to the dry
370 sample (Figure 6e) and the model therefore does not fit it as well. However the shear-mode
371 attenuation (Figure 6f) is reasonably well reproduced.

372



373

374 **Figure 6.** The measured moduli and attenuation for the dry and glycerine saturated sample
 375 BS-V5 at 5 MPa effective stress determined from both axial and hydrostatic oscillations
 376 together with the results of the analytical solutions (AS) for the drained-undrained transition
 377 and squirt flow.

378

379 **Table 2.** Rock and fluid properties for the simple isotropic squirt flow model for sample BS-
 380 V5 subjected to an effective stress of 5 MPa.

	Parameters	Symbol	Model Input
Fluid	Fluid Bulk Modulus	K_f	4.36 GPa
	Viscosity	η	1.087 Pa s
Rock	Stiff Porosity	ϕ_s	0.2213

Compliant Porosity	ϕ_c	1.55×10^{-4}
Grain Bulk Modulus	K_g	36 GPa
Drained Bulk Modulus	K_d	9.2 GPa
Drained Shear Modulus	G_d	9.1 GPa
High Pressure Bulk Modulus	K_h	13.3 GPa
Crack aspect ratio	α	0.0025

381

382

383 **Table 3.** Rock and fluid properties for the 1D-model of the drained-undrained transition for

384 sample BS-V5 subjected to an effective stress of 5 MPa.

	Parameter	Symbol	Model Input
Fluid	Fluid Bulk Modulus	K_f	4.36 GPa
	Viscosity	η	1.087 Pa s
Rock	Length	L	0.083 m
	Diameter	D	0.04 m
	Porosity	ϕ	0.2215
	Permeability	κ	58.7 mD
	Grain Bulk Modulus	K_g	36 GPa
	Drained Bulk Modulus	K_d	9.2 GPa
Dead Volume	Dead Volume	$V_{dead\ vol.}$	$26 \times 10^{-6} \text{ m}^3$

385

386 3.4 Comparison with previous experimental results

387

388 Our experiments are very similar to those performed by Mikhaltsevitch *et al.* (2015; 2016),

389 also on a glycerine-saturated Berea sandstone sample. Their sample D had a permeability of

390 71 mD, a porosity of 19 %, and while mainly composed of quartz (80 %) and feldspar (12 %)

391 also had substantial amounts of kaolinite (8 %), making it very similar to our sample BS-V5.

392 In their study, the forced axial oscillation measurements were performed on both the dry and

393 glycerine-saturated sample at 10 MPa effective stress. Under glycerine saturation the pore

394 pressure was maintained at 3 MPa. The measurements were also performed at different
395 temperatures ranging from 23 to 31 °C. For the sake of comparing our data to theirs we will
396 only consider the measurements performed at 23 °C. Mikhaltsevitch *et al.* (2015) are
397 confident that their measurements are performed under undrained conditions, based on
398 Gassmann's predictions, matching well their measured bulk modulus at low frequencies.
399 They interpret the observed frequency-dependent attenuation to be in response to squirt flow.

400

401 In Figure 7 we compare the Young's modulus and attenuation measured in the dry and
402 glycerine-saturate sample D of Mikhaltsevitch *et al.* (2016) (Figure 7a and b) to that measured
403 in our sample BS-V5 (Figure 7c and d). It is important to note that we are showing our
404 measurements performed at 5 MPa effective stress, because we did not perform
405 measurements at 10 MPa effective stress. However, as seen in section 3.2 we observed that
406 increasing the effective stress reduces the attenuation amplitude but does not result in a large
407 shift of the attenuation peaks with respect to frequency. While sample D is more
408 compressible, under dry conditions it is less attenuating than sample BS-V5, which could
409 indicate a minor dependence of our sample on the strain amplitude (e.g. Gordon and Davis
410 1968; Winkler *et al.* 1979). However frequency-dependent attenuation in response to wave-
411 induced fluid flow should be approximately independent of strain (Tisato and Quintal 2014).
412 Mikhaltsevitch *et al.* (2016) observe the attenuation peak that they attribute to squirt flow at
413 ~0.4 Hz (Figure 7b), while for our sample the attenuation peak we attribute to squirt flow is at
414 >10 Hz (Figure 7d). A shift of the attenuation peak by 1 to 2 orders of magnitude can be
415 explained by a minor variation in the characteristic crack aspect ratio of the sample, given that
416 the characteristic frequency of squirt flow is proportional to the cube of the aspect ratio
417 (O'Connell and Budiansky 1977; Gurevich *et al.* 2010).

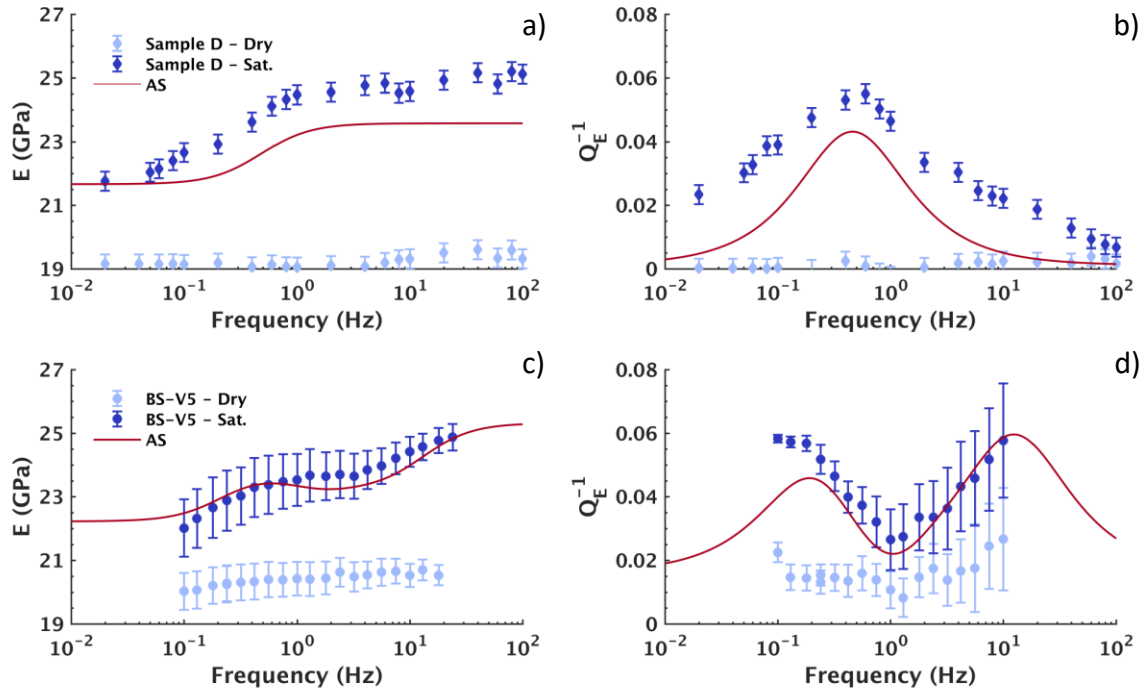
418

419 Included in Figure 7a and b we show the result of Gurevich *et al.*'s (2010) squirt flow model.
420 As input parameters we use the bulk and shear modulus and porosity of the dry sample D
421 (Mikhaltsevitch *et al.* 2015). The other rock parameters for the model were not available,
422 therefore the other parameters are the same as for sample BS-V5 (Table 2), with the exception
423 of the crack aspect ratio which is again used as a fitting parameter. Both the Young's modulus
424 (Figure 7a) and the attenuation (Figure 7b) are underestimated by the analytical solution,
425 which is possibly related to the choice of the high-pressure bulk modulus that controls the
426 bulk modulus dispersion. Mikhaltsevitch *et al.* 2015 show the frequency dependent bulk
427 modulus inferred from the measured Young's modulus and Poisson's, which is highly
428 dispersive and which the analytical solution cannot account for with the choice of parameters.
429 An important aspect of the analytical solution is that it does not account for a distribution of
430 aspect radii and therefore the asymptote of attenuation at low frequencies scales as $Q^{-1} \propto f$,
431 while at high frequencies scales as $Q^{-1} \propto f^{-1}$ (Gurevich *et al.* 2010). The comparison between
432 the measured attenuation and result of the analytical indicates that the sample D indeed has a
433 distribution of aspect radii as would be expected (e.g. Cheng and Toksöz 1979, Subramanyan
434 *et al.* 2015). In sample BS-V5 (Figures 7c and d) it is not clear whether the sample has a
435 narrower distribution in aspect radii, given that the attenuation curve is only partially
436 observed.

437

438 Berea sandstone has been extensively studied in the past and it contains substantial amounts
439 of clay, which fills pores and coats grains (e.g. Kareem *et al.* 2017). Christensen and Wang
440 (1985) observed an increase in compressional wave velocities and a decrease in shear wave
441 velocities with pore pressure in water saturated Berea sandstone, attributing the observations
442 to the high compressibility of clays that make up parts of the cement. Zoback and Byerlee
443 (1975) also attribute the compressibility of clay to the increase in permeability with increasing

444 pore pressure in Berea sandstone. At seismic frequencies Pimienta *et al* (2017) observe a
445 sensitivity of the frequency dependent Poisson ratio to fluid pressure in a Berea sandstone
446 sample saturated with a glycerine-water mixture. They apply different fluid pressures up to 9
447 MPa at a constant effective stress of 1 MPa, however they do not elaborate on what may be
448 inducing the increase in Poisson's ratio with fluid pressure. Although the experiments carried
449 out in our study are very similar to those of Mikhaltsevitch *et al.* (2016) in terms of rock type,
450 fluid properties and the range of effective stresses applied, the fluid pressure was 4 MPa in
451 sample BS-V5 and 3 MPa for sample D. The difference in fluid pressure is not very large,
452 however, for future research on squirt flow as an attenuation mechanism, the impact of
453 changes in fluid pressure could be very interesting because of the sensitivity of squirt flow to
454 crack aspect ratio. In Berea sandstone, where clays coat grains, a variation in fluid pressure at
455 constant effective stress could facilitate a change in crack aspect ratio, which could in turn be
456 identified in the measured frequency dependence of attenuation and modulus dispersion.
457



458

459 **Figure 7.** a) Young's modulus and b) attenuation Q_E^{-1} for the dry and glycerine-saturated
 460 Berea sandstone (sample D) measured at 10 MPa effective stress by Mikhaltsevitch et al.
 461 (2016), together with the results of the analytical solution (AS) for squirt flow. For
 462 comparison, c) the Young's modulus and d) attenuation Q_E^{-1} of the dry and glycerine-
 463 saturated sample BS-V5 at 5 MPa effective stress, together with the results of the analytical
 464 solutions for the drained-undrained transition and squirt flow.

465

466 4. Conclusions

467

468 We performed hydrostatic and axial forced oscillations experiments on a dry and glycerine-
 469 saturated Berea sandstone sample. In the glycerine saturated sample the measured attenuation
 470 is frequency dependent with an attenuation peak at ~ 0.1 Hz and a second, partial, peak
 471 beginning at ~ 3 Hz. The first attenuation peak is in response to fluid pressure diffusion from
 472 the sample into the pore fluid lines, referred to as the drained-undrained transition. The
 473 second partial attenuation peak is likely in response to squirt flow, resulting from microscopic

474 heterogeneities in the compressibility of the porous solid frame of the rock. The fit of
475 analytical solutions for the drained-undrained transition and squirt flow satisfactorily
476 reproduced the measured attenuation and moduli. A comparison with independently
477 conducted experiments on a very similar sample under comparable conditions appears to
478 confirm the sensitivity of squirt flow to variations in the characteristic aspect ratios of the
479 compliant porosity.

480

481 **Acknowledgments**

482

483 This work is supported by a grant from the Swiss National Science Foundation. We thank
484 Marie Violay for access to the EPFL Laboratory of Experimental Rock Mechanics, Laurent
485 Gastaldo for coring the samples from the source blocks and Lucas Pimienta for doing the
486 porosity measurements. We thank Jean-Pierre Burg for access to the ETH Zurich Rock
487 Deformation Laboratory and Claudio Madonna for helping with the sample preparation. The
488 data for this paper are available by contacting the authors.

489

490 **References**

491

492 Adam L., Batzle M. and Brevik I. 2006, Gassmann fluid substitution and shear modulus
493 variability in carbonates at laboratory seismic and ultrasonic frequencies. *Geophysics*, 71,
494 F173-F183.

495

496 Adelinet M., Fortin J., Gueguen Y., Schubnel A. and Geoffroy L. 2010. Frequency and fluid
497 effects on elastic properties of basalt: Experimental investigations. *Geophysical Research*
498 *Letters*, 37, L02303.

499

500 Adelinet M., Fortin J. and Gueguen Y. 2011. Dispersion of elastic moduli in a porous-cracked
501 rock: Theoretical predictions for squirt-flow. *Tectonophysics*, 503, 173-181.

502

503 Batzle M. L., Han D.-H. and Hofmann R. 2006. Fluid mobility and frequency-dependent
504 seismic velocity - Direct measurements. *Geophysics*, 71, N1-N9.

505

506 Borgomano J. V. M., Pimienta L., Fortin J. and Gueguen Y. 2017. Dispersion and attenuation
507 measurements of elastic moduli of a dual-porosity limestone. *Journal of Geophysical*
508 *Research: Solid Earth*, 122, doi:10.1002/2016JB013816.

509

510 Chapman M., Zatspin S. V. and Crampin S. 2002. Derivation of a microstructural poroelastic
511 model. *Geophysical Journal International*, 151, 427-451.

512

513 Cheng C. H. and Toksöz M. N. 1979. Inversion of Seismic Velocities for the Pore Aspect
514 Ratio Spectrum of Rock. *Journal of Geophysical Research*, 84, 7533-7543.

515

516 Christensen N. I. and Wang H. F. 1985. The influence of pore pressure and confining pressure
517 on dynamic elastic properties of Berea sandstone. *Geophysics*, 50, 207-213.

518

519 Collet O. and Gurevich B. 2016. Frequency dependence of anisotropy in fluid saturated rocks
520 – Part II: Stress-induced anisotropy case. *Geophysical Prospecting*, 64, 1085-1097.

521

522 David E. C., Fortin J., Schubnel A., Gueguen Y. and Zimmerman R. W. 2013. Laboratory
523 measurements of low- and high-frequency elastic moduli in Fontainebleau sandstone.
524 Geophysics, 78, D369-D379.

525

526 Dunn K.-J. 1987. Sample boundary effect in acoustic attenuation of fluid-saturated porous
527 cylinders. Journal of the Acoustical Society of America, 81, 1259-1266.

528

529 Gardner G. H. F. 1962. Extensional waves in fluid-saturated porous cylinders. Journal of the
530 Acoustical Society of America, 34, 36-40.

531

532 Gassmann F. 1951. Über die Elastizität poröser Medien: Vierteljahrsschrift der
533 Naturforschenden Gesellschaft in Zürich, 96, 1-23.

534 Gurevich B., Makaryska D., de Paula O. S. and Pervukhina M. 2010. A simple model for
535 squirt-flow dispersion and attenuation in fluid-saturated granular rocks. Geophysics, 75, 6.

536

537 Gordon R. B. and Davis L. A. 1968, Velocity and Attenuation of Seismic Waves in
538 Imperfectly Elastic Rock. Journal of Geophysical Research, 73, 3917-3935.

539

540 Hart D. J. and Wang H. F. 1999. Pore pressure and confining stress dependence of poroelastic
541 linear compressibilities and Skempton's B coefficient for Berea sandstone. American Rock
542 Mechanics Association, 37th US Rock Mechanics Symposium.

543

544 Johnston D. H., Toksöz M. N. and Timur A. 1979. Attenuation of seismic waves in dry and
545 saturated rocks: II. Mechanisms. Geophysics, 44, 691-711.

546

547 Kareem R., Cubillas P., Gluyas J., Bowen L., Hillier S. and Greenwell H. C. 2017, Multi-
548 technique approach to the petrophysical characterization of Berea sandstone core plugs
549 (Cleveland Quarries, USA). *Journal of Petroleum Science and Engineering*, 147, 436-455.

550

551 Masson Y. J. and Pride S. R. 2007. Poroelastic finite difference modeling of seismic
552 attenuation and dispersion due to mesoscopic-scale heterogeneity. *Journal of Geophysical*
553 *Research*, 112, B03204, doi:10.1029/2006JB004592.

554

555 Masson Y. J. and Pride S. R. 2011. Seismic attenuation due to patchy saturation. *Journal of*
556 *Geophysical Research*, 116, B03206, doi:10.1029/2010JB007983.

557

558 Mavko G. and Jizba D. 1991. Estimating grain-scale fluid effects on velocity dispersion in
559 rocks. *Geophysics*, 56, 1940-1949.

560

561 McKavanagh B. and Stacey F.D. 1974. Mechanical hysteresis in rocks at low strain
562 amplitudes and seismic frequencies. *Physics of the Earth and Planetary Interiors*, 8, 246–250.

563

564 Mikhaltsevitch V., Lebedev M. and Gurevich B. 2015. A laboratory study of attenuation and
565 dispersion effects in glycerol-saturated Berea sandstone at seismic frequencies. SEG, doi:
566 <http://dx.doi.org/10.1190/segam2015-5898429.1>.

567

568 Mikhaltsevitch V., Lebedev M. and Gurevich B. 2016. Validation of the laboratory
569 measurements at seismic frequencies using the Kramers-Kronig relationship. *Geophysical*
570 *Research Letters*, 43, 4986-4991.

571

572 Mörig R. and Burkhardt H. 1989. Experimental evidence for the Biot-Gardner theory.
573 Geophysics, 54, 524-527.
574

575 Müller T. M., Toms-Stewart J. and Wenzlau F. 2008. Velocity-saturation relation for partially
576 saturated rocks with fractal pore fluid distribution. Geophysical Research Letters, 35, L09306.
577

578 O'Connell R. J. and Budiansky B. 1977. Viscoelastic Properties of Fluid-Saturated Cracked
579 Solids. Journal of Geophysical Research, 5719-5735.
580

581 O'Connell R. J. and Budiansky B. 1978. Measures of dissipation in viscoelastic media.
582 Geophysical Research Letters, 5, 5-8.
583


584 Pimienta L., Fortin J. and Guéguen Y. 2015a. Experimental study of Young's modulus
585 dispersion and attenuation in fully saturated sandstones. Geophysics, 80, L57-L72.
586

587 Pimienta L., Fortin J. and Guéguen Y. 2015b. Bulk modulus dispersion and attenuation in
588 sandstones. Geophysics, 80(2), D111-D127, doi: 10.1190/geo2014-0335.1.
589

590 Pimienta L., Borgomano J. V. M., Fortin J. and Guéguen Y. 2016a. Modelling the
591 drained/undrained transition: effect of the measuring method and the boundary conditions.
592 Geophysical Prospecting, 64, 1098-1111.

593 Pimienta, L., Fortin J., Guéguen Y. 2016b [Effect of fluids and frequencies on Poisson's ratio](#)
594 [of sandstone samples](#) Geophysics 81 (2), D183-D195
595

596 Pimienta L., Borgomano J. V. M., Fortin J. and Guéguen Y. 2017, Elastic Dispersion and
597 Attenuation in Fully Saturated Sandstones: Role of Mineral Content, ^[L]Porosity, and

598 Pressures. *Journal of Geophysical Research: Solid Earth*, 122, 9950–9965. 

599

600 Pride S. R., Berryman J. G. and Harris J. M. 2004. Seismic attenuation due to wave-induced
601 flow. *Journal of Geophysical Research*, 109, B01201.

602

603 Spencer, J. W. and Shine J. 2016. Seismic wave attenuation and modulus dispersion in
604 sandstones. *Geophysics*, 81, D211-D231.

605

606 Subramaniyan S., Quintal B., Madonna C. and Saenger E. H. 2015. Laboratory-based seismic
607 attenuation in Fontainebleau sandstone: Evidence of squirt flow. *Journal of Geophysical
608 Research: Solid Earth*, 120, 7526-7535.

609

610 Tisato N. and Quintal B. 2013. Measurements of seismic attenuation and transient fluid
611 pressure in partially saturated Berea sandstone: evidence of fluid flow on the mesoscopic
612 scale, *Geophysical Journal International*, 195, 342-351.

613

614 Tisato N. and Quintal B. 2014. Laboratory measurements of seismic attenuation in
615 sandstone: Strain versus fluid saturation effects, *Geophysics*, 79, WB9–WB14.

616

617 Walsh J. B. 1965. The Effects of Cracks on the Compressibility of Rock. *Journal of
618 Geophysical Research*, 70, 381-389.

619

620 Winkler K., Nur A. and Gladwin M. 1979, Friction and seismic attenuation in rocks. *Nature*,
621 277, 528-531.

622

623 Zoback, M. D. and Byerlee, J. D. 1975. Permeability and effective stress. Bulletin - American
624 Association of Petroleum Geologists, 59, 154-158.

625

626